Nanoscale

Visualizing Formation of High Entropy Alloy Nanoparticles with Liquid Phase Transmission Electron Microscopy

Journal:	*Nanoscale*
Manuscript ID	NR-ART-03-2023-001073.R2
Article Type:	Paper
Date Submitted by the Author:	05-Jun-2023
Complete List of Authors:	Sun, Jiayue; University of Maryland Leff, Asher; Army Research Laboratory Li, Yue; University of Maryland Woehl, Taylor; University of Maryland

Visualizing Formation of High Entropy Alloy Nanoparticles with Liquid Phase Transmission Electron Microscopy

Jiayue Sun,[1] Asher Leff,[2,3] Yue Li,[1] Taylor J. Woehl[4*]

[1.] Department of Chemistry and Biochemistry, University of Maryland, College Park, MD 20742, United States

[2.] Army Research Directorate, Combat Capabilities Development Command, Army Research Laboratory, Adelphi, MD 20783, United States

[3.] General Technical Services, LLC, Wall Township, New Jersey 07727, United States

[4.] Department of Chemical and Biomolecular Engineering, University of Maryland, College Park, MD 20742, United States

* Corresponding author: tjwoehl@umd.edu

ABSTRACT

High entropy alloy (HEA) nanoparticles hold promise as active and durable (electro)catalysts. Understanding their formation mechanism will enable rational control over composition and atomic arrangement of multimetallic catalytic surface sites to maximize their activity. While prior reports have attributed HEA nanoparticle formation to nucleation and growth, there is a dearth of detailed mechanistic investigations. Here we utilize liquid phase transmission electron microscopy (LPTEM), systematic synthesis, and mass spectrometry (MS) to demonstrate that HEA nanoparticles form by aggregation of cluster intermediates. AuAgCuPtPd HEA nanoparticles are synthesized by aqueous co-reduction of metal salts with sodium borohydride in the presence of thiolated polymer ligands. Varying the metal:ligand ratio during synthesis showed that alloyed HEA nanoparticles formed only above a threshold ligand concentration. Interestingly, stable single metal atoms and sub-nanometer clusters are observed by TEM and MS in the final HEA nanoparticle solution, suggesting nucleation and growth is not the dominant mechanism. Increasing supersaturation ratio increased particle size, which together with observations of stable single metal atoms and clusters, supported an aggregative growth mechanism. Direct real-time observation with LPTEM imaging showed aggregation of HEA nanoparticles during synthesis. Quantitative analyses of the nanoparticle growth kinetics and particle size distribution from LPTEM movies were consistent with a theoretical model for aggregative growth. Taken together, these results are consistent with a reaction mechanism involving rapid reduction of metal ions into sub-nanometer clusters followed by cluster aggregation driven by borohydride ion induced thiol ligand desorption. This work demonstrates the importance of cluster species as potential synthetic handles for rational control over HEA nanoparticle atomic structure.

INTRODUCTION

High entropy alloys (HEAs) are distinct from conventional dilute alloys containing minor fractions of metal dopants as they contain near equimolar amounts of five or more metals stabilized by high mixing entropy.[1-3] Initial work on bulk HEAs demonstrated enhanced functional properties compared to dilute alloys, including high strength and melting temperature due to sluggish atomic diffusion and lattice strain.[4, 5] The recent discovery of HEA nanoparticles has led to demonstrations of their great potential for catalysis,[6-9] energy storage and conversion,[10-12] and mechanical property enhancement.[13] However, synthesis of nanoscale HEAs containing immiscible metals is challenging due to the thermodynamic driving force for phase separation due to differing crystal structure, atomic size, valence electron configuration, and electronegativity.[14] Seminal work by the Hu group circumvented this challenge by utilizing rapid solid-state synthesis, termed carbothermal shock synthesis, which involved millisecond heating of metal precursor salt mixtures followed by rapid temperature quenching.[15] In recent years, a number of solid state synthesis methods for HEA nanoparticles made their debut such as electrosynthesis,[16, 17] fast-moving bed pyrolysis,[18] laser ablation,[19, 20] aerosol synthesis,[21] and microwave heating synthesis.[22] In general, these prior synthesis routes used high temperature and rapid temperature quenching to generate kinetically trapped HEA nanostructures. Previous researchers have suggested that HEA nanoparticles form by classical nucleation and growth mechanism during thermal synthesis. Gao *et al.* described HEA nanoparticle formation during rapid pyrolysis using Lamer's burst nucleation model, where the high synthesis temperature decreased critical nuclei size and free energy barrier to nucleation.[18] Recent work has shown that the formation of HEAs is in part driven by energetically favorable short-range order, which forms metal cluster species with different atomic arrangements.[23]

Solution phase HEA nanoparticle synthesis methods include solvothermal synthesis,[24-27] thermal annealing of core-shell nanoparticles,[28] sonochemical synthesis,[29] and oil-phase synthesis.[30] Similar to the solid-state synthesis approaches, these methods used strong chemical reductants or high temperature to rapidly convert metal precursors into HEA nanoparticles and are thought to involve classical nucleation and growth. For instance, Broge *et al.* concluded formation of HEA nanoparticles during solvothermal synthesis occurred *via* nucleation and autocatalytic growth.[25] Despite some success in forming HEA nanoparticles, solution phase co-reduction often leads to phase separation of metals and must be carefully optimized to produce fully alloyed nanoparticles, which is a slow empirical process. Rational solution phase synthesis of HEA nanoparticles with tailored composition and highly active multimetallic catalytic sites in a timely manner will require enhanced fundamental understanding of the formation mechanisms of HEA nanoparticles.

While prior work has suggested classical nucleation and growth mediate metal nanoparticle formation during synthesis, there is a growing body of literature suggesting alternative particle attachment-based mechanisms. Among these prior works, many researchers have emphasized the existence and importance of nanoclusters as key intermediates during nanoparticle synthesis.[31, 32] Liquid phase transmission electron microscopy (LPTEM) has been indispensable in unraveling non-classical nanoparticle formation mechanisms as it allows direct real time visualization of reaction intermediates and their interactions by processes such as aggregation and coalescence. Prior LPTEM work has directly visualized a number of nonclassical nanoparticle growth pathways, such as oriented attachment,[33-37] aggregative growth,[38] precursor-dense liquid phase mediated growth,[39-42] and multistage mechanisms involving coalescence, Ostwald ripening, and monomer attachment.[43, 44] Here we utilize synchronous solution chemistry and LPTEM to uncover the

formation mechanism for HEA nanoparticles formed by rapid aqueous phase co-reduction. Specifically, we interrogate the growth mechanism of HEA nanoparticles during co-reduction of aqueous metal salts with sodium borohydride ($NaBH_4$) in the presence of thiolated polymer ligands. While thiol ligands are known to strongly bind nanoparticle surfaces, borohydride anions have been demonstrated to readily displace thiolated molecules from metal surfaces and cause nanoparticle aggregation.[45] Our results demonstrate that borohydride induced desorption of thiol ligands destabilizes intermediate clusters, which causes cluster-cluster aggregation that forms HEA nanoparticles. In contrast to all prior studies on the formation mechanisms of HEA nanoparticles, this work indicates that in this case HEA nanoparticles did not form by a nucleation and growth mechanism but instead by aggregative growth. This work emphasizes the importance of intermediate clusters as synthetic handles for the controlled synthesis of HEA nanoparticles.[32]

EXPERIMENTAL SECTION

Chemicals

Gold(III) chloride trihydrate ($HAuCl_4 \cdot 3H_2O$, ≥99.9% trace metals basis), silver nitrate ($AgNO_3$, ACS reagent, ≥99.0%), copper(II) sulfate pentahydrate ($CuSO_4 \cdot 5H_2O$, ACS reagent, ≥98.0%), potassium platinum(II) chloride (K_2PtCl_4, ≥99.9% trace metals basis), potassium palladium(II) chloride (K_2PdCl_4, ≥99.9% trace metals basis), poly(ethylene glycol) methyl ether thiol (mPEG-SH, average molecular weight of 1000 g/mol), and sodium borohydride ($NaBH_4$, powder, ≥98.0%) were purchased from Sigma Aldrich and used as received. Type II DI water (18.2 MΩ cm) was used for all experiments.

Solution chemistry synthesis

Briefly, HEA particles were synthesized by first mixing metal salts specified in the previous section in equimolar concentrations with mPEG-SH ligands at the specified concentration. The precursor was reduced under vigorous magnetic stirring with $NaBH_4$ in water. For example, a sample with 1:1 molar ratio of metal ions to mPEG-SH ligands was prepared by adding 36 μL of a 20 mM stock solution of each metal salt to 4 mL DI water with stirring, followed by 180 μL of 20 mM PEG-SH. This yielded a total metal ion concentration of 0.86 mM, with each metal ion present in equimolar concentration. When varying the metal:ligand ratio or the reducing agent:metal ratio, the total metal ion concentration and composition were held constant at this value and the ligand or reducing agent concentration adjusted accordingly. The reaction solution was then reduced immediately by addition of 450 μL 20 mM $NaBH_4$, which gave a concentration of 1.94 mM $NaBH_4$ in the final reaction solution. The reaction was stirred in air at room temperature for 1 hour to allow $NaBH_4$ to fully react and hydrolyze. HEA particles were washed by water at 7500 rpm for 10 mins three times by using VWR® centrifugal filters (molecular weight cut-off 10 kDa).

TEM characterization

5 μL of HEA nanoparticle solution was drop cast onto carbon-coated aluminum TEM grids (Ted Pella 01844A). Excess liquid in the droplet was removed by wicking with a Kimwipe to encourage uniform coverage of nanoparticles on the carbon after drying. Samples were plasma cleaned in an air plasma for 30 seconds prior to imaging. High resolution scanning transmission electron microscopy (HR-STEM) and energy dispersive x-ray spectroscopy (EDS) were

performed on a JEOL ARM200F TEM equipped with an Oxford XMAX TLE 100 windowless EDS spectrometer operating at 200 kV acceleration voltage. EDS spectra and maps were quantified using the Cliff-Lorimer equation. STEM imaging for particle size distribution measurements was performed on a JEOL JEM-2100F TEM operating at 200 kV acceleration voltage. Nanoparticle size distributions were measured from hundreds of nanoparticles for each sample using an automated image analysis algorithm written in MATLAB.

MALDI-TOF mass spectrometry

HEA nanoparticle reaction solutions were characterized by matrix assisted laser desorption ionization time of flight mass spectrometry (MALDI-TOF MS, Bruker AutoFlex). Mass spectra were acquired in negative linear TOF mode over a detection range of $m/z = 100 - 2000$. A 10 µL HEA sample solution was mixed with 10 µL 2',6'-Dihydroxyacetophenone (DHA) (97%, Sigma Aldrich) matrix (10 mg/mL) and 2 µL of the mixture was drop cast on the MALDI target plate (MTP 384 ground steel BC) without further purification and dilution. The MALDI-TOF MS was equipped with smartbeam-II solid state laser and the laser power was set to reach 100% with a laser frequency of 500 Hz.

LPTEM experiments

LPTEM experiments were performed in a MEMS-based microfluidic sample holder (Protochips, USA). The sample cell creates an electron transparent liquid sample by sandwiching a thin liquid film between two free-standing 50 nm silicon nitride films supported on silicon chips.[46] Before assembling the sample cell, both silicon chips were rinsed in acetone and methanol

followed by drying with compressed gas and air plasma treatment (Harrick Plasma, PDC-32G) for 3 minutes to remove residual organic contamination and render them hydrophilic. A small droplet of sample precursor (~0.5 μL) was sandwiched between the two chips and hermetically sealed in the sample holder tip by a series of o-rings, creating an electron transparent window that was 50 x 50 μm in size. Flow spacers with a thickness of 500 nm defined the liquid flow channel, but silicon nitride film bulging leads to a nominal liquid thickness of ~750 nm as measured by electron energy loss spectroscopy in a previous study.[47] After the cell was assembled, precursor solution was flowed through the microfluidic lines in the sample holder for ~30 minutes at a flow rate of 300 µL/hr to remove any bubbles.

The precursor solution for LPTEM was a dilute version of the flask synthesis recipe.[48] 2.4 µL of 20 mM metal salt precursor solutions of each metal were added to 8 mL water and gently vortexed for 5 seconds followed by addition of 18 µL (1:1.5 metal:ligand) or 24 µL (1:2 metal:ligand) of 20 mM mPEG-SH ligand solution followed by vortexing. The final metal concentration in the precursor was 0.03 mM and the ligand concentration varied from 0.045 mM to 0.050 mM. All water used for precursor preparation for LPTEM was degassed for 1 h by sonication (Branson, CPX2800H), followed by 30 minutes of nitrogen purging to minimize oxygen content and bubbling during experiments. LPTEM experiments were performed on a JEOL JEM-2100F TEM operating at 200 kV accelerating voltage in STEM mode. The dose rate $\dot{d}$, a measure of the amount of energy deposited in the liquid sample, was documented for each *in situ* movie, defined as $\dot{d} = \frac{i_e s}{e A}$, where i_e $\left(\mathrm{C/s}\right)$ is the electron beam current, e is electron charge, s is the density normalized stopping power of water $\left(s = 2.798 \times 10^5 \,\mathrm{eV}\frac{\mathrm{m}^2}{\mathrm{kg}}\right)$ at 200 kV and A is the STEM image area.[47, 49, 50] The dose rate $\left(\mathrm{MGy/s} = 10^6 \frac{\mathrm{J}}{\mathrm{kg \cdot s}}\right)$ is indicated for each LPTEM

experiment in the article. After LPTEM experiments the liquid cell was disassembled and the reaction solution was air dried onto the silicon nitride surface. The nanoparticles and metal clusters were characterized by HR-STEM and EDS using a JEOL ARM200F operating at 200 kV. Tracking individual nanoparticle growth kinetics was performed manually in ImageJ (**Fig. S1**) while particle size distribution (PSD) tracking was performed using a custom MATLAB script that used standard image segmentation to track particle area and number of particles as a function of time.

RESULTS AND DISCUSSION

HEA nanoparticles were synthesized by $NaBH_4$ reduction of $AuCl_4^-$, Ag^+, Cu^{2+}, $PtCl_4^{2-}$, $PdCl_4^{2-}$ ions in the presence of mPEG-SH ligands. Polymers with thiol anchoring groups are well-known strongly binding metal nanoparticle ligands that have been used to synthesize monometallic silver,[51] gold,[52] copper,[53, 54] platinum,[55, 56] and palladium nanoparticles.[57] Further, thiol ligands are well known to stabilize metal nanoclusters,[58-60] which prior works have indicated can be essential intermediates to the formation of alloyed nanoparticles.[48, 61] The rapid reduction of all metal precursors by $NaBH_4$ is anticipated to minimize internal electron transfer and mitigate preferential reduction of metal ions with high reduction potential.[16] **Fig. 1a-c** shows representative HR-STEM images of HEA nanoparticles formed by co-reduction of Au, Ag, Cu, Pt, and Pd metal salts. The resulting nanoparticles ranged in diameter from 0.5 – 3 nm and were both single and polycrystalline (**Fig. 1a,** inset). High angle annular dark field (HAADF) STEM images, which display atomic number (Z) image contrast proportional to Z^2, showed random variations in the atomic column intensity in the nanoparticles that are indicative of a random alloy. Some nanoparticles showed sub-nanometer scale phase separation, denoted by locally lower image contrast corresponding to lower average atomic number (red arrow in **Fig. 1c**). HEA nanoparticles

formed by solvothermal synthesis showed similar nanoscale phase separation.[28] Interestingly, the nanoparticles co-existed with sub-nanometer, non-crystalline metal clusters (**Fig. 1d, Fig. S2,** and **Fig. S3**). Similar to the HEA nanoparticles showing variations in the HAADF-STEM intensity, the variable intensities of single atoms and atoms in small clusters indicated they contained different elements. The range of HAADF-STEM atom intensities in the clusters were consistent with the expected range for Z-contrast imaging of the five metals (**Fig. S3**).

Fig. 1e shows a MALDI-TOF MS spectra of the reaction solution taken immediately after nanoparticle synthesis, which showed species with molecular weights in the expected range for few atom multimetallic clusters. MS simulations showed that several peaks in the spectra were consistent with multimetallic clusters adducts containing either hydrogen or boron (**Fig. S4**). Despite the affinity of mPEG-SH to metals, we did not observe any mPEG-SH protected metal clusters with MALDI-TOF or electrospray ionization mass spectrometry (ESI-MS). However, we infer that the clusters observed by MALDI-TOF and HAADF-STEM were initially ligated by mPEG-SH due to their stability in colloidal solution. It is likely mPEG-SH protected metallic clusters were either not efficiently ionized or the laser desorption ionization destroyed the complex; prior work has shown that MALDI-TOF can desorb thiol ligands from nanoparticle surfaces.[62] We could not characterize the oxidation state of the clusters independent of the nanoparticle phase, but prior x-ray characterization and modeling has shown similar thiol ligand capped clusters are metallic in nature.[61, 63]

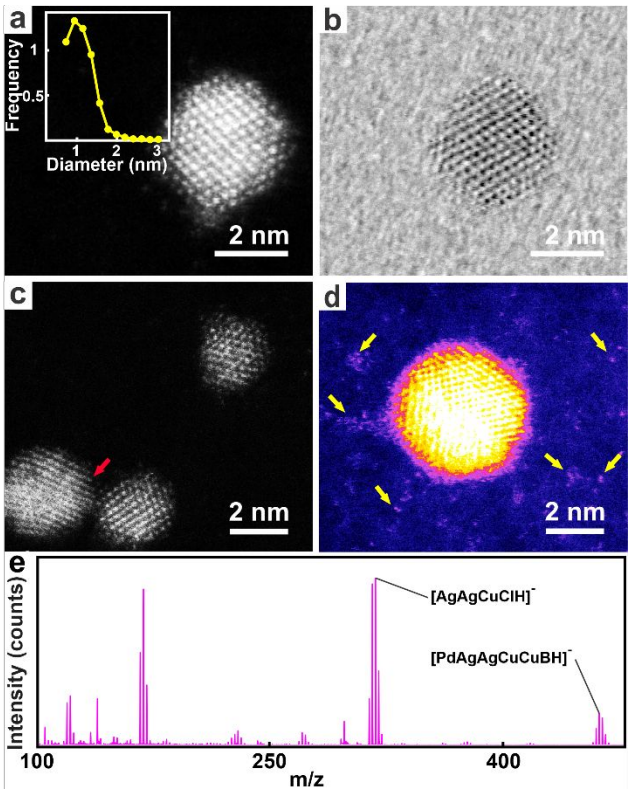

Fig. 1. HR-STEM and MALDI-TOF MS characterization of HEA nanoparticles synthesized by aqueous phase co-reduction. (a-c) HAADF-STEM images of HEA nanoparticles synthesized with a metal:ligand ratio of 1:1. The inset in (a) shows the PSD of the nanoparticles measured from HAADF-STEM images. The red arrow in (c) points to a sub-nanometer phase separated domain. (d) HAADF-STEM image of an HEA nanoparticle surrounded by sub-nanometer clusters and free atoms. The image is false colored and contrast adjusted to highlight the clusters and atoms (yellow arrows). (e) MALDI-TOF MS spectrum of metal clusters in an HEA nanoparticle solution prepared with a metal:ligand ratio of 1:1.

The metal:ligand ratio during nanoparticle synthesis was systematically varied to explore the effect on alloying and size. **Fig. 2** shows representative atomic resolution HAADF-STEM and STEM energy dispersive x-ray (STEM-EDS) compositional maps for nanoparticles produced with 1:1, 2.5:1, and 5:1 metal:ligand molar ratios. HAADF-STEM images showed that nanoparticles

formed with 1:1 and 2.5:1 metal:ligand ratios were a mixture of polycrystalline and single crystal nanoparticles (**Figs. 2a,b**). Conversely, some nanoparticles formed with a 5:1 metal:ligand ratio were not HEAs and exhibited aggregation and phase separation into core-shell nanoparticles (**Fig. 2c**). Additional images showing the range of particle types formed are included in **Fig. S5**. STEM-EDS of nanoparticles synthesized with 1:1 (**Fig. 2d**) and 2.5:1 (**Fig. 2e**) metal:ligand ratios showed that the five metals were uniformly distributed in the HEA nanoparticles within the spatial resolution of EDS mapping (~0.5 nm). EDS quantification of HEA compositions for 1:1 and 2.5:1 ratios revealed the nanoparticles contained (by mass) 31.7 ± 2.9% Au, 6.1 ± 2.1% Ag, 14.4 ± 1.2% Cu, 29 ± 2.7% Pt, 18.7 ± 2.2% Pd and 62.2 ± 2.2% Au, 1 ± 1.0% Ag, 17 ± 1.1% Cu, 6.3 ± 1.6% Pt, and 13.5 ± 1.4% Pd, respectively (Additional EDS quantifications of HEA particles are shown in **Table S1**). Together with HAADF-STEM images, the EDS mapping and composition measurements showed that the 1:1 metal:ligand ratio formed nanoparticles containing all five metals with uniform metal spatial distributions and random alloyed structures, consistent with HEA nanoparticles formed by other synthesis methods.[18, 28] The 2.5:1 metal:ligand ratio contained four of the metals with a nearly negligible silver concentration. We note that some metals were deficient in the nanoparticles compared to the initial precursor composition due to preferential metal reduction. STEM-EDS showed that some nanoparticles synthesized with 5:1 metal:ligand ratio were a mixture of phase separated particles, with Au, Cu, and Pt preferentially segregated to the nanoparticle cores, and small nanoparticles containing only Pd and Ag (**Fig. 2f**). As such, we did not classify these nanoparticles as HEAs.

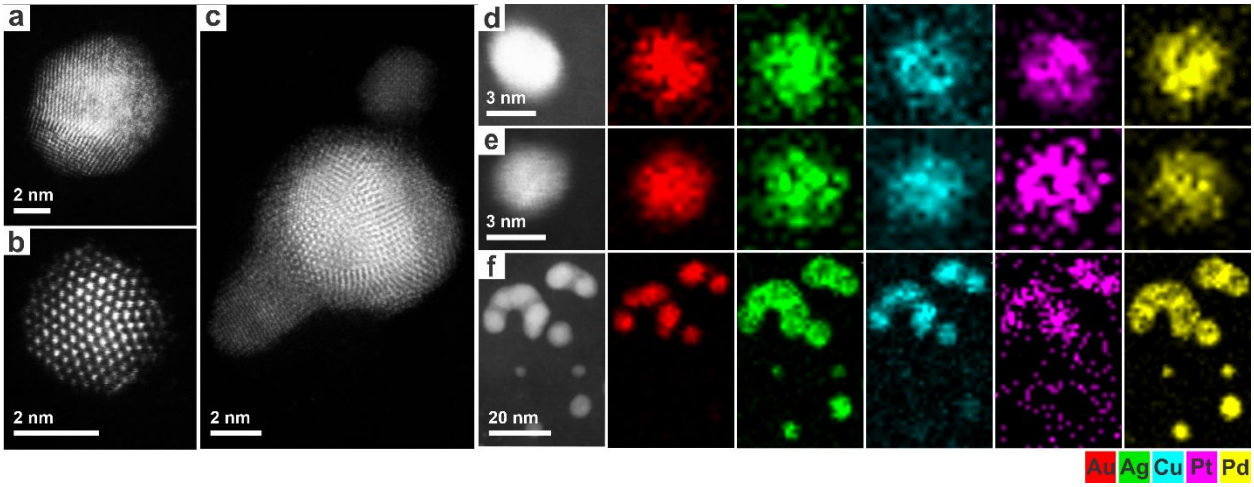

Fig. 2. Atomic structure and elemental mapping of HEA nanoparticles. (a-c) HAADF-STEM images of HEA particles synthesized with metal:ligand ratios of (a) 1:1, (b) 2.5:1, and (c) 5:1. (d-f) HAADF-STEM images (first column) and EDS elemental maps of HEA nanoparticles synthesized with metal:ligand ratios of (d) 1:1, (e) 2.5:1, and (f) 5:1.

From the particle size distributions (PSD) in **Fig. 3**, we noticed an increase in the average particle size with decreasing ligand concentration (see **Fig. S6** for STEM images used to measure the PSD). Prior work has shown that decreasing the thiol ligand concentration leads to more rapid aggregation and growth due to low surface ligand coverage at early reaction times.[64] The ligand concentration also impacts metal reduction rate and alloying. Prior work showed that sulfur ligand coordination to metal ions during co-reduction encourages alloying by effecting simultaneous reduction of each metal ion type.[61] Thiol ligands react with metal ions to form metal thiolates, which reduce at a similar rate across all metals; if insufficient thiol ligand is present, some metal ions remain coordinated with water or halides, leading to disparate reduction rates. This phenomenon likely explains the formation of phase separated particles at high metal to ligand ratios in this work.

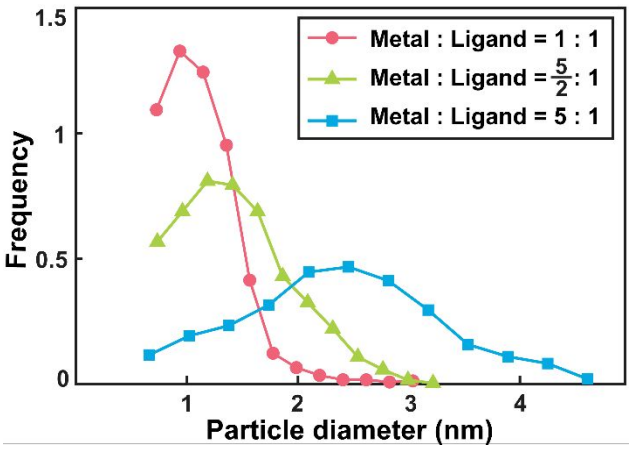

Fig. 3. PSD of nanoparticles synthesized with different metal:ligand ratios.

HEA nanoparticle formation was directly visualized in real time with *in situ* LPTEM synthesis using aqueous electrons (e_{aq}^{-}) as the reducing agent. While there are chemical differences between the redox properties of aqueous electrons and $NaBH_4$, prior work by Wang *et al.* showed that LPTEM can visualize formation of alloyed metal nanoparticles with thiolated polymer ligands with similar reaction kinetics compared to solution chemical synthesis with $NaBH_4$.[48] The present work utilizes a different precursor solution containing 5 metal ions instead of gold and copper ions only, but we expect the electron beam chemistry to be qualitatively similar to the prior work on AuCu nanoparticles. This prior study showed that AuCu nanoparticles synthesized by electron dose controlled aqueous electron reduction and $NaBH_4$ reduction had statistically similar size distribution, morphology, and composition. Notwithstanding, there are several differences between these two reduction methods that bear mentioning. The standard reduction potential of the aqueous electron is more negative ($E^0 = -2.3\ V$) than borohydride ions ($E^0 = -0.48\ V$), resulting in a thermodynamic driving force for silver ion reduction by aqueous electrons that is about three times larger than for $NaBH_4$.[46] Accordingly, prior work showed that diluting the metal ion concentration by a factor of ~30 led to

growth of individual nanoparticles at a similar rate during LPTEM and $NaBH_4$ reduction.[48] Similar to the previous work, we utilized lower metal:ligand ratios than solution chemical synthesis to scavenge hydroxyl radicals that can oxidize metals and desorb ligands *via* oxidative elimination.[48, 65, 66] Solution pH can be affected by the electron beam due to production of hydronium ions; however, prior models have shown the pH is not significantly reduced for the low pH of the precursor solution (pH ≈ 4).[67] Despite these differences, the qualitative processes that occur during reduction by $NaBH_4$ and aqueous electrons are expected to be similar. Most importantly, both strong reducing agents rapidly reduce all available metal ions to metal atoms within seconds, which suggests similar chemical processes will control subsequent nanoparticle formation.

Fig. 4a and **Fig. 4b** show time-lapsed LPTEM images of HEA nanoparticle formation with 1:1.5 and 1:2 metal:ligand ratios, respectively. While sub-nanometer clusters are certainly important for the nanoparticle formation mechanism, they are not directly visualized here as the spatial resolution is limited to ~1 nm. Prior work in our lab showed that imaging alloyed nanoparticle formation at uncontrolled dose rate led to preferential reduction of certain metals and particle destabilization by electron beam damage,[48] so the magnification and spatial resolution in these experiments was intentionally lower to reduce these effects. The *in situ* image frames shown in **Fig. 4a** and **Fig. 4b** were acquired at dose rates of 362 MGy/s and 212 Mgy/s, which yielded similar aqueous electron concentrations of 5.77 μM and 4.39 μM as determined by the radiolysis model by Schneider et al (See Supplementary Video 1 and Supplementary Video 2 for full data sets, see **Table S2** for aqueous electron concentrations corresponding to all dose rates used in this work).[67] In each experiment, nearly spherical nanoparticles with sizes of 5 – 10 nm were observed to form over times of 30 – 60 seconds. Nanoparticles in each sample grew individually separated by a few nanometers within larger agglomerates of 10 – 20 nanoparticles. While particles exhibited

more aggregation in **Fig. 4b**, they still grew isotropically and individually from each other with clear interparticle separation. We tracked the size of ten particles as a function of time between two experiments at nearly the same dose rate. Four of the tracked particles are denoted by arrows in **Fig. 4a** and **Fig. 4b** and their growth trajectories are shown in log space in **Fig. 4c** (additional trajectories are shown in **Fig. S7**). The nanoparticle diameters (d) were observed to increase with a $d \sim t^{1/3}$ power law after about 10 s, which could be consistent with either diffusion limited growth[68] or aggregative growth.[38] Growth trajectory measurements absent other supporting experiments cannot conclusively determine the growth mechanism.[38] We compared the PSD of the resulting HEA nanoparticles shown in **Fig. 4b** and those prepared by solution chemistry with theoretical PSD models for diffusion limited growth, reaction limited growth, and aggregative growth and found that in each case, the aggregative growth PSD had the smallest statistical deviation from the experimental PSDs (**Fig. S8** and **Table S3**).

Following LPTEM synthesis, we disassembled and dried the liquid cell for HAADF-STEM and STEM-EDS characterization **(Fig. 4d)**. While EDS is possible in the liquid phase, we do not get sufficient signal on our TEM to characterize such small particles. To increase the EDS signal, the reaction solutions was dried on the microchip surface followed by gentle rinsing with water; nanoparticles and clusters remained attached to the dried silicon nitride surface after rinsing because the nanoparticles formed on the membrane surface.[69] Similar to the HEA nanoparticles synthesized by $NaBH_4$ reduction, HAADF-STEM characterization displayed that the *in situ* synthesized HEA particles were crystalline **(Fig. 4e)** and co-existed with sub-nanometer sized clusters **(Fig. 4f)**. STEM-EDS elemental mapping revealed the *in situ* synthesized HEA particles contained all five elements with similar composition as the 1:1 metal:ligand ratio prepared by

$NaBH_4$ reduction (65 ± 1.5% Au, 10 ± 0.8% Ag, 16 ± 0.5% Cu, 5 ± 1.2% Pt, and 4 ± 0.8% Pd) **(Fig. 4g)**.

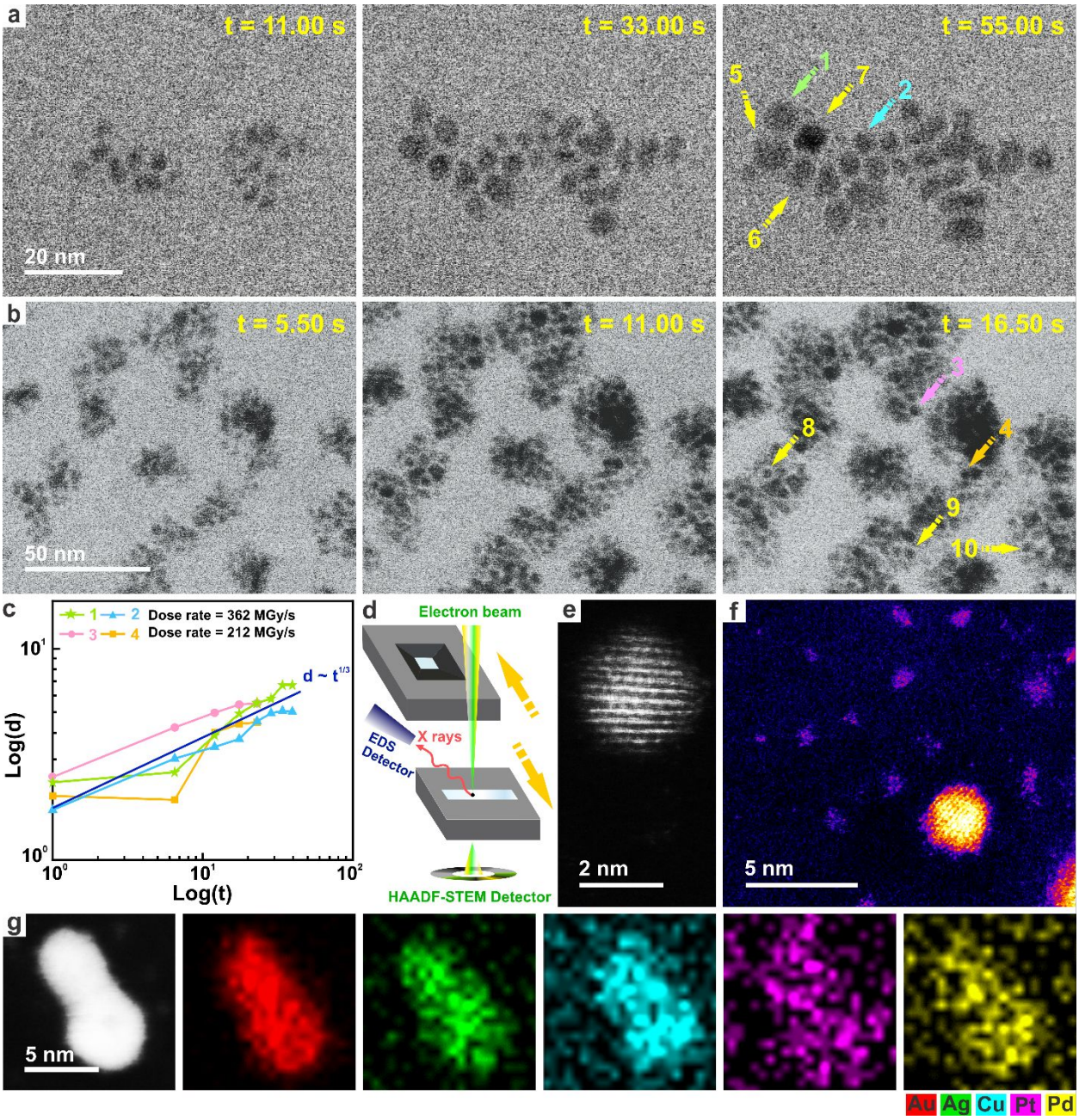

Fig. 4. LPTEM visualization of HEA nanoparticle formation dynamics. (a-b) Time-lapsed LPTEM images of HEA nanoparticle growth (a) at a magnification of 2,000,000 × (beam current = 23 pA, dose rate = 362 Mgy/s) with a metal:ligand ratio of 1:1.5, and (b) 1,500,000 × (beam current = 23

pA, dose rate = 212 Mgy/s) with a metal:ligand ratio of 1:2. The images have been cropped to enhance particle visibility. (c) Double logarithmic plot of the particle diameter (d) as a function of time (t). The particles are denoted by numbers 1 to 4 in **Fig. 4a** and **Fig. 4b**. Particle size vs. time data for particles denoted by numbers 5 – 10 are shown in **Fig. S7**. (d) Schematic of HAADF-STEM and STEM-EDS on the disassembled and dried liquid cell window. (e) Dry state HAADF-STEM image of an HEA particle formed by LPTEM synthesis. (f) False colored dry state HAADF-STEM image of an HEA particle formed by LPTEM synthesis surrounded by sub-nanometer clusters. (g) Dry state HAADF-STEM image and EDS elemental maps of an HEA nanoparticle synthesized by LPTEM.

LPTEM synthesis using precursors containing a higher metal:ligand ratio of 1.5:1 (less ligand than in **Fig. 4**) showed significant aggregation as opposed to growth of individual nanoparticles (**Fig. 5**). Nanoparticles did not display clear interparticle spacing and instead large agglomerates grew as single monoliths (**Fig. 5a**) or by nanoparticle attachment to their surfaces (**Fig. 5b**). Prior work in our lab showed that excessive aggregation of alloyed nanoparticles as seen here was due to large hydroxyl radicals concentration, which caused ligand desorption or intermolecular crosslinking.[48, 66] Taken together, the results of the LPTEM experiments were qualitatively consistent with the solution phase synthesis, where small individual nanoparticles formed at relatively higher ligand concentration and aggregated nanoparticles formed as the ligand concentration was decreased.

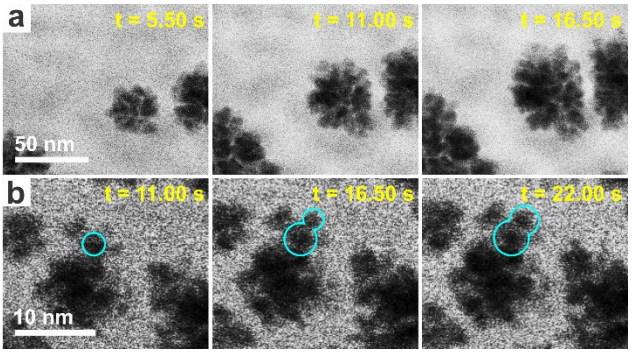

Fig. 5. LPTEM visualization of HEA nanoparticle aggregation dynamics. (a-b) Time-lapsed LPTEM images of HEA nanoparticle aggregation and growth with a metal:ligand ratio of 1.5:1 at (a) a magnification of 1,500,000 × (beam current = 23 pA, dose rate = 212 MGy/s) and (b) at a magnification of 800,000 × (beam current = 74 pA, dose rate = 205 MGy/s). Blue circles in (b) denote an example of particle aggregation. Images have been cropped to enhance visibility of dynamics.

Based on the experimental results so far, we consider potential formation mechanisms for HEA nanoparticles during rapid chemical reduction in aqueous solution. Prior work has suggested that HEA nanoparticles formed during solid state synthesis by Lamer's model of burst nucleation followed by monomer attachment.[18] In Lamer's model, particle formation is initiated by rapid nucleation following a rapid transient spike in metal atom supersaturation ratio.[70] Classical nucleation theory is typically used to describe the nucleation step, where the positive free energy associated with creating a new solid-liquid interface creates a nucleation free energy barrier and critical nuclei size. Aggregates of metal atoms with sizes below the critical nuclei size spontaneously dissolve while clusters above the critical nuclei size grow *via* monomer attachment. Once nucleation is initiated and the growth phase occurs, single metal atoms or clusters are unstable and will spontaneously grow into nanoparticles. Two testable predictions emerge from classical nucleation theory and Lamer's model: (1) single atoms should not be stable or exist in

the final reaction solution because they are inherently unstable once nanoparticle growth is initiated and (2) particle size should decrease with increasing supersaturation ratio due to formation of more and smaller nuclei.[71] Our observation of stable single atoms and clusters after synthesis is inconsistent with the first prediction, suggesting that nucleation does not govern the initial phase of nanoparticle formation.

Synthesis experiments varying the $NaBH_4$ concentration as a proxy for supersaturation ratio tested the effect of supersaturation on particle size against the second prediction of Lamer's model (**Fig. 6**; images used to generate the PSDs are shown in **Fig. S9**). Increasing the $NaBH_4$ concentration increases the metal atom supply rate to solution and therefore the initial supersaturation ratio.[72] Particle size and size dispersity increased as a function of $NaBH_4$ concentration for a constant metal:ligand ratio with average particle size increasing from 1.2 nm to 1.7 nm when increasing $NaBH_4$ concentration from 0.42 mM to 7.0 mM (**Fig. 6a**). Measurements of the particle eccentricity ($\epsilon = 1$ for a circle, $\epsilon = 0$ for a line, $0 < \epsilon < 1$ are ellipses), indicated that particles became less circular with increasing $NaBH_4$ concentration due to particle aggregation (**Fig. 6b**).[48] Taken together, the increase in particle size with increasing reducing agent concentration and supersaturation ratio is inconsistent with Lamer's model and nucleation as the rate limiting step for nanoparticle formation, indicating an alternate mechanism is at play.

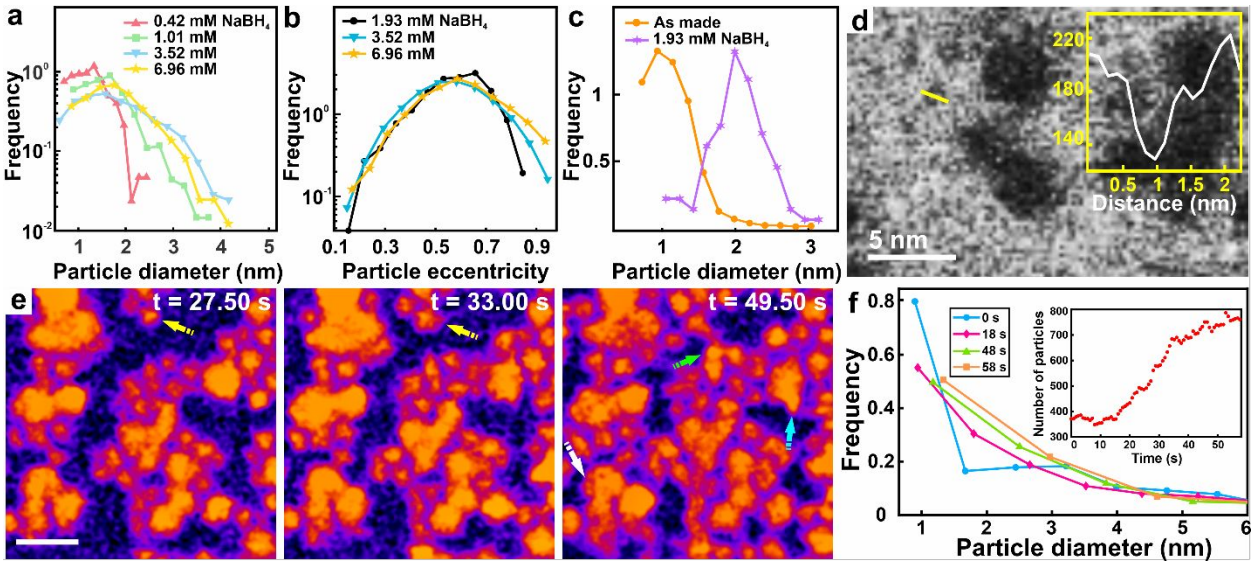

Fig. 6. Systematic HEA nanoparticle synthesis and LPTEM observation of nanoparticle aggregation are consistent with an aggregative growth mechanism. (a) PSDs and (b) eccentricity distributions of HEA particles synthesized with different $NaBH_4$ concentrations. (c) PSD of preformed HEA particles before and after addition of 1.93 mM $NaBH_4$. (d) Bright field STEM image showing a sub-nanometer cluster in a LPTEM image. The inset shows the intensity profile across the yellow line drawn along the metal cluster. (e) Time-lapsed LPTEM images showing growth and aggregation of preformed HEA nanoparticles (1:1 metal:ligand ratio) with no metal precursor present at a magnification of 1,500,000× (beam current = 74 pA, dose rate = 682 MGy/s). The images have been cropped and false colored to highlight aggregation of small nanoparticles and clusters. The scale bar is 10 nm. (f) PSD of the nanoparticles in (e) as a function of time. The inset shows the number of particles in the image as a function of time.

The observation of increased particle aggregation and size with increasing $NaBH_4$ concentration suggests that the reducing agent plays a role aside from simply reducing the metal ions during nanoparticle formation here. Indeed, prior density functional theory calculations showed that the hydride-gold surface bond energy is about 50% larger than a gold thiolate bond.[45]

Prior work has reported that borohydride can displace ligands including thiolated polymers (PEG-SH),[73] 4-aminothiophenol (4-ATP),[74] polyvinylpyrrolidone (PVP),[75, 76] and oleylamine (OAm).[76] Ligand removal from nanoparticles by hydride and borohydride ions led to nanoparticle aggregation in most literature observations. The small size of hydride ligands allows nanoparticles to closely approach each other, where attractive Van der Waals interactions cause irreversible nanoparticle attachment. Polte *et al.* suggested that borohydride ion induced ligand desorption led to secondary aggregation after initial metal cluster formation.[70] To further test whether $NaBH_4$ induces aggregation we measured the PSD of preformed HEA nanoparticles before and after addition of $NaBH_4$ (**Fig. 6c**). The average nanoparticle size increased by a factor of nearly two after $NaBH_4$ addition, which is consistent with borohydride and hydride ions displacing the mPEG-SH ions during nanoparticle synthesis to drive aggregation.

Companion LPTEM experiments were performed to directly observe the aggregation of preformed HEA nanoparticles due to ligand desorption. Here HEA nanoparticles dispersed in water with no metal ions in solution were imaged by LPTEM. Hydroxyl radicals generated by radiolysis caused mPEG-SH ligand displacement *via* oxidative elimination,[66] which destabilized nanoparticles similar to $NaBH_4$ addition. **Fig. 6f** shows that continuous LPTEM imaging of pre-formed nanoparticles caused additional nanoparticles to appear in the image area and drove their growth and aggregation over time (see Supplementary Video 3 and Supplementary Video 4). The nanoparticle PSD at early times showed high concentrations of ~1 nm clusters and nanoparticles ranging up to 6 nm in size (**Fig. 6g**). Particles continuously accumulated in the image area, likely due to the presence of strong electric fields generated by the electron beam (**Fig. 6g, inset**).[77] Time dependent PSDs showed that ~1 nm clusters were consumed over time to form larger particles. Some nanoparticles were observed to increase their size by self-growth (yellow arrows, **Fig. 6f**),

which absent metal ion precursors must result from attachment of metal clusters below the ~1 nm spatial resolution of LPTEM. Aggregation of ≥ 1 nm clusters and nanoparticles was observed in several instances, where clusters attached to larger nanoparticles or each other (arrows in **Fig. 6f**). While LPTEM imaging here has a resolution limited to about 1 nm and could not directly resolve the clusters as shown by dry state HAADF-STEM imaging, the continuous aggregation and growth of nanoparticles provides strong supporting evidence for cluster aggregation during synthesis. These data, complemented by solution chemistry, mass spectrometry, and LPTEM growth rate and PSD analysis, provide strong evidence for a mechanism involving ligand desorption induced cluster aggregation.

Scheme 1 summarizes the mechanism for the formation of HEA nanoparticles. First, metal ions complexed by mPEG-SH ligands were rapidly reduced by $NaBH_4$ to form metal atoms and metal clusters ligated by mPEG-SH. Interestingly, these single atoms and sub-nanometer clusters were observed in the nanoparticle solution, indicating that absent $NaBH_4$ the clusters were stable for at least several days. In the next step, excess borohydride and hydride ions competed for binding sites on the sub-nanometer clusters with mPEG-SH. Borohydride and hydride ions displaced mPEG-SH ligands on single atoms and clusters and caused growth by aggregation. Over time, the colloidal stability of the metal clusters increased with their increasing size and at the same time the borohydride ion concentration decreased due to hydrolysis and oxidation.[70] Eventually, a steady state distribution of nanoparticles, metal clusters, and single metal atoms stabilized by mPEG-SH ligands was established. Experiments showed that metal nanocluster intermediates did not contain all five metals; however, random aggregation of these clusters resulted in HEA nanoparticles containing all the metals. Increasing the $NaBH_4$ concentration relative to the mPEG-SH concentration led to increased binding rates of borohydride and hydride ions to the

nanoparticles and thus enhanced aggregation, leading to larger particle sizes. Likewise, increasing the metal:ligand ratio (*e.g.*, 5:1 metal:ligand) created a large concentration of metal ions that were not complexed to thiol ligands, which led to preferential reduction of certain metals and phase separation. Instead of nucleation acting as the kinetically limiting step for nanoparticle formation the rate limiting step for nanoparticle formation here was cluster aggregation mediated by desorption of mPEG-SH ligands from the nanoparticle surface by borohydride and hydride ions.

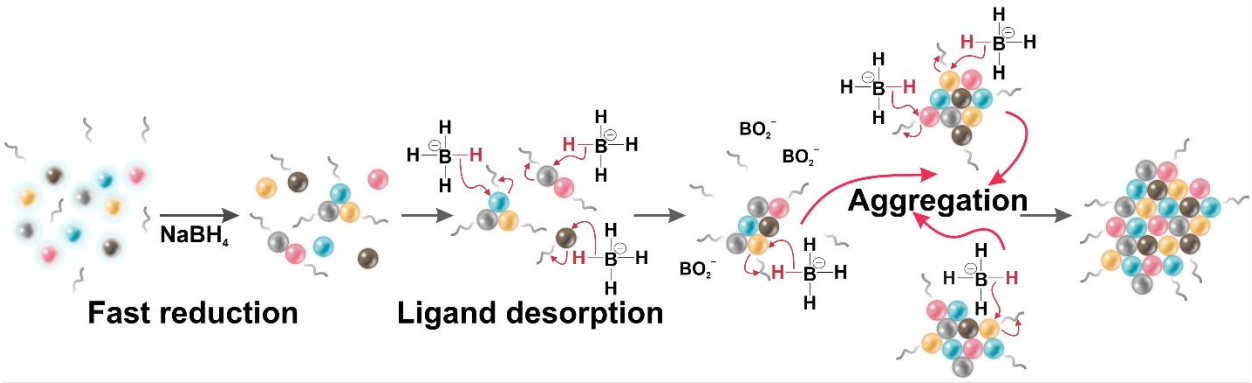

Scheme 1. Reaction mechanism for HEA nanoparticle formation.

CONCLUSIONS

This work combined systematic synthesis, particle size analysis, MS, and advanced LPTEM characterization to explore the formation mechanism of HEA nanoparticles during aqueous phase co-reduction. While prior work has suggested that classical nucleation theory and Lamer's model explain HEA nanoparticle formation, our experiments pointed to a growth mechanism involving ligand desorption induced aggregation of metal clusters together with monomer attachment. We demonstrated a threshold ligand concentration was required to form HEA nanoparticles, which was likely due to the need to convert all metal ions to metal thiolates, which reduce at similar rates. Quantitative analysis of LPTEM nanoparticle growth kinetics and PSD shape and direct LPTEM observations of nanoparticle aggregation were broadly consistent

with an aggregative growth mechanism. These results suggest future avenues for rational synthesis of HEA nanoparticles by controlling the composition and molecular structure of intermediate metal clusters. One potential avenue could involve controlling the composition and molecular makeup of metal cluster intermediates and their aggregation during synthesis to enrich the surface of HEA nanoparticle catalysts with multimetallic active sites.[32] Another approach, which has been demonstrated for quantum dots,[31] could involve synthesizing HEA nanoparticles using intermediate metal clusters as precursors to enhance control over alloy composition.

Author Contributions

T. J. W. conceived of and supervised the study. J. S. performed liquid phase TEM experiments and solution phase synthesis, TEM imaging, and data analysis. J. S. and Y. L. performed mass spectrometry. A. L. performed atomic resolution STEM and EDS characterization. T. J. W. and J. S. prepared the manuscript.

Conflicts of Interest

The authors declare no competing financial interest.

Acknowledgment

This material is based upon work supported by the National Science Foundation under grant no. 2045258. We thank Dr. S. C. Liou and Dr. W. A. Chiou for their assistance with electron microscopy work in AIMLAB and Prof. Chunsheng Wang for use of his glove box to store

chemicals. This collaborative work was sponsored in part by the U.S. Army Combat Capabilities Development Command - Army Research Laboratory and was accomplished under an ARL Cooperative Research and Development Agreement (CRADA 14-052-22).

References

1. J. W. Yeh, S. K. Chen, S. J. Lin, J. Y. Gan, T. S. Chin, T. T. Shun, C. H. Tsau and S. Y. Chang, *Adv. Eng. Mater.*, 2004, **6**, 299-303.
2. B. Cantor, I. T. H. Chang, P. Knight and A. J. B. Vincent, *Mater. Sci. Eng. A*, 2004, **375**, 213-218.
3. J. W. Yeh, *Ann. Chim.: Sci. Mater.* 2006, **31**, 633-648.
4. Y. Zou, H. Ma and R. Spolenak, *Nat. Commun.*, 2015, **6**, 7748.
5. Z. M. Li, K. G. Pradeep, Y. Deng, D. Raabe and C. C. Tasan, *Nature*, 2016, **534**, (7606), 227-230.
6. Y. Xin, S. H. Li, Y. Y. Qian, W. K. Zhu, H. B. Yuan, P. Y. Jiang, R. H. Guo and L. B. Wang, *Acs Catal.*, 2020, **10**, 11280-11306.
7. D. S. Wu, K. Kusada, T. Yamamoto, T. Toriyama, S. Matsumura, S. Kawaguchi, Y. Kubota and H. Kitagawa, *J. Am. Chem. Soc.*, 2020, **142**, 13833-13838.
8. Y. F. Sun and S. Dai, *Sci. Adv.*, 2021, **7**.
9. Y. G. Yao, Q. Dong, A. Brozena, J. Luo, J. W. Miao, M. F. Chi, C. Wang, I. G. Kevrekidis, Z. J. Ren, J. Greeley, G. F. Wang, A. Anapolsky and L. B. Hu, *Science*, 2022, **376** (6589), eabn3103.
10. P. F. Xie, Y. G. Yao, Z. N. Huang, Z. Y. Liu, J. L. Zhang, T. Y. Li, G. F. Wang, R. Shahbazian-Yassar, L. B. Hu and C. Wang, *Nat. Commun.*, 2019, **10**, 4011.
11. H. D. Li, Y. Han, H. Zhao, W. J. Qi, D. Zhang, Y. D. Yu, W. W. Cai, S. X. Li, J. P. Lai, B. L. Huang and L. Wang, *Nat. Commun.*, 2020, **11**, 5437.
12. A. Amiri and R. Shahbazian-Yassar, *J. Mater. Chem. A*, 2021, **9**, 782-823.
13. Z. Q. Fu, L. Jiang, J. L. Wardini, B. E. MacDonald, H. M. Wen, W. Xiong, D. L. Zhang, Y. Z. Zhou, T. J. Rupert, W. P. Chen and E. J. Lavernia, *Sci. Adv.*, 2018, **4**, eaat8712.
14. X. J. Chang, M. Q. Zeng, K. L. Liu and L. Fu, *Adv. Mater.*, 2020, **32**, 1907226.
15. Y. G. Yao, Z. N. Huang, P. F. Xie, S. D. Lacey, R. J. Jacob, H. Xie, F. J. Chen, A. M. Nie, T. C. Pu, M. Rehwoldt, D. W. Yu, M. R. Zachariah, C. Wang, R. Shahbazian-Yassar, J. Li and L. B. Hu, *Science*, 2018, **359**, 1489-1494.
16. M. W. Glasscott, A. D. Pendergast, S. Goines, A. R. Bishop, A. T. Hoang, C. Renault and J. E. Dick, *Nat. Commun.*, 2019, **10**, 2650.
17. J. Sure, D. Sri Maha Vishnu, H.-K. Kim and C. Schwandt, *Angew. Chem. Int. Ed.*, 2020, **59**, 11830-11835.
18. S. J. Gao, S. Y. Hao, Z. N. Huang, Y. F. Yuan, S. Han, L. C. Lei, X. W. Zhang, R. Shahbazian-Yassar and J. Lu, *Nat. Commun.*, 2020, **11**, 2016.
19. C. W. Bing Wang, Xiwen Yu, Yuan Cao, Linfeng Gao, Congping Wu, Yingfang Yao, Zhiqun Lin & Zhigang Zou, *Nat. Synth.*, **2022**, **1**, 138-146.
20. F. Waag, Y. Li, A. R. Ziefuss, E. Bertin, M. Kamp, V. Duppel, G. Marzun, L. Kienle, S. Barcikowski and B. Goekce, *Rsc Adv.*, 2019, **9**, 18547-18558.
21. Y. Yang, B. A. Song, X. Ke, F. Y. Xu, K. N. Bozhilov, L. B. Hu, R. Shahbazian-Yassar and M. R. Zachariah, *Langmuir*, 2020, **36**, 1985-1992.
22. H. Y. Qiao, M. T. Saray, X. Z. Wang, S. M. Xu, G. Chen, Z. N. Huang, C. J. Chen, G. Zhong, Q. Dong, M. Hong, H. Xie, R. Shahbazian-Yassar and L. B. Hu, *Acs Nano*, 2021, **15**, 14928-14937.

23. S. Chen, Z. H. Aitken, S. Pattamatta, Z. X. Wu, Z. G. Yu, D. J. Srolovitz, P. K. Liaw and Y. W. Zhang, *Nat. Commun.*, 2021, **12**, 4953.
24. M. Bondesgaard, N. L. N. Broge, A. Mamakhel, M. Bremholm and B. B. Iversen, *Adv. Funct. Mater.*, 2019, **29**, 1905933.
25. N. L. N. Broge, M. Bondesgaard, F. Sondergaard-Pedersen, M. Roelsgaard and B. B. Iversen, *Angew. Chem. Int. Ed.*, 2020, **59**, 21920-21924.
26. K. Huang, B. W. Zhang, J. S. Wu, T. Y. Zhang, D. D. Peng, X. Cao, Z. Zhang, Z. Li and Y. Z. Huang, *J. Mater. Chem. A*, 2020, **8**, 11938-11947.
27. D. S. Wu, K. Kusada, Y. Nanba, M. Koyama, T. Yamamoto, T. Toriyama, S. Matsumura, O. Seo, I. Gueye, J. Kim, L. S. R. Kumara, O. Sakata, S. Kawaguchi, Y. Kubota and H. Kitagawa, *J. Am. Chem. Soc.*, 2022, **144**, 3365-3369.
28. Y. F. Chen, X. Zhan, S. L. A. Bueno, I. H. Shafei, H. M. Ashberry, K. Chatterjee, L. Xu, Y. W. Tang and S. E. Skrabalak, *Nanoscale Horiz.*, 2021, **6**, 231-237.
29. F. Okejiri, Z. Z. Yang, H. Chen, C. L. Do-Thanh, T. Wang, S. Z. Yang and S. Dai, *Nano Res.*, 2022, **15**, 4792-4798.
30. D. Zhang, Y. Shi, H. Zhao, W. J. Qi, X. L. Chen, T. R. Zhan, S. X. Li, B. Yang, M. Z. Sun, J. P. Lai, B. L. Huang and L. Wang, *J. Mater. Chem. A*, 2021, **9**, 889-893.
31. D. C. Gary, M. W. Terban, S. J. L. Billinge and B. M. Cossairt, *Chem. Mater.*, 2015, **27**, 1432-1441.
32. A. Loiudice and R. Buonsanti, *Journal*, *Nature Synthesis* **2022**, **1**, 344-351.
33. D. S. Li, M. H. Nielsen, J. R. I. Lee, C. Frandsen, J. F. Banfield and J. J. De Yoreo, *Science*, 2012, **336**, 1014-1018.
34. J. M. Yuk, J. Park, P. Ercius, K. Kim, D. J. Hellebusch, M. F. Crommie, J. Y. Lee, A. Zettl and A. P. Alivisatos, *Science*, 2012, **336**, 61-64.
35. Z. Aabdin, J. Y. Lu, X. Zhu, U. Anand, N. D. Loh, H. B. Su and U. Mirsaidov, *Nano Lett.*, 2014, **14**, 6639-6643.
36. C. Zhu, S. X. Liang, E. H. Song, Y. J. Zhou, W. Wang, F. Shan, Y. T. Shi, C. Hao, K. B. Yin, T. Zhang, J. J. Liu, H. M. Zheng and L. T. Sun, *Nat. Commun.*, 2018, **9**.
37. W. Wei, H. T. Zhang, W. Wang, M. Dong, M. Nie, L. T. Sun and F. Xu, *Acs Appl. Mater. Interfaces*, 2019, **11**, 24478-24484.
38. T. J. Woehl, C. Park, J. E. Evans, I. Arslan, W. D. Ristenpart and N. D. Browning, *Nano Lett.*, 2014, **14**, 373-378.
39. N. D. Loh, S. Sen, M. Bosman, S. F. Tan, J. Zhong, C. A. Nijhuis, P. Kral, P. Matsudaira and U. Mirsaidov, *Nat. Chem.*, 2017, **9**, 77-82.
40. J. Yang, J. Koo, S. Kim, S. Jeon, B. K. Choi, S. Kwon, J. Kim, B. H. Kim, W. C. Lee, W. B. Lee, H. Lee, T. Hyeon, P. Ercius and J. Park, *J. Am. Chem. Soc.*, 2019, **141**, 763-768.
41. W. Dachraoui, D. Keller, T. R. Henninen, O. J. Ashton and R. Erni, *Nano Lett.*, 2021, **21**, 2861-2869.
42. G. Li, N. N. He, J. X. Deng, J. X. Liu, Y. Sun, M. Qu, Y. H. Jiang, T. Q. Zhao, S. Y. Zhou, H. B. Zeng, Q. Z. Zheng, H. G. Liao and S. G. Sun, *Cryst. Growth Des.*, 2021, **21**, 6025-6030.
43. D. Keller, T. R. Henninen and R. Erni, *Nanoscale*, 2020, **12**, 22511-22517.
44. W. Dachraoui, T. R. Henninen, D. Keller and R. Erni, *Sci. Rep.*, 2021, **11**.
45. S. M. Ansar, F. S. Arneer, W. F. Hu, S. L. Zou, C. U. Pittman and D. M. Zhang, *Nano Lett.*, 2013, **13**, 1226-1229.
46. T. J. Woehl, *Chem. Mater.*, 2020, **32**, 7569-7581.
47. M. Wang, C. Park and T. J. Woehl, *Chem. Mater.*, 2018, **30**, 7727-7736.
48. M. Wang, A. C. Leff, Y. Li and T. J. Woehl, *Acs Nano*, 2021, **15**, 2578-2588.
49. T. J. Woehl, J. E. Evans, L. Arslan, W. D. Ristenpart and N. D. Browning, *Acs Nano*, 2012, **6**, 8599-8610.
50. D. Alloyeau, W. Dachraoui, Y. Javed, H. Belkahla, G. Wang, H. Lecoq, S. Ammar, O. Ersen, A. Wisnet, F. Gazeau and C. Ricolleau, *Nano Lett.*, 2015, **15**, 2574-2581.

51. C. P. Joshi, M. S. Bootharaju, M. J. Alhilaly and O. M. Bakr, *J. Am. Chem. Soc.*, 2015, **137**, 11578-11581.
52. S. Takano and T. Tsukuda, *J. Am. Chem. Soc.*, 2021, **143**, 1683-1698.
53. W. T. Wei, Y. Z. Lu, W. Chen and S. W. Chen, *J. Am. Chem. Soc.*, 2011, **133**, 2060-2063.
54. X. Gao, S. He, C. Zhang, C. Du, X. Chen, W. Xing, S. Chen, A. Clayborne and W. Chen, *Adv. Sci*, 2016, **3**.
55. C. Yee, M. Scotti, A. Ulman, H. White, M. Rafailovich and J. Sokolov, *Langmuir*, 1999, **15**, 4314-4316.
56. D. Pedone, M. Moglianetti, E. De Luca, G. Bardi and P. P. Pompa, *Chem. Soc. Rev.*, 2017, **46**, 4951-4975.
57. M. Cargnello, N. L. Wieder, P. Canton, T. Montini, G. Giambastiani, A. Benedetti, R. J. Gorte and P. Fornasiero, *Chem. Mater.*, 2011, **23**, 3961-3969.
58. X. Kang, Y. W. Li, M. Z. Zhu and R. C. Jin, *Chem. Soc. Rev.*, 2020, **49**, 6443-6514.
59. Y. X. Du, H. T. Sheng, D. Astruc and M. Z. Zhu, *Chem. Rev.*, 2020, **120**, 526-622.
60. R. C. Jin, G. Li, S. Sharma, Y. W. Li and X. S. Du, *Chem. Rev.*, 2021, **121**, 567-648.
61. L. E. Marbella, D. M. Chevrier, P. D. Tancini, O. Shobayo, A. M. Smith, K. A. Johnston, C. M. Andolina, P. Zhang, G. Mpourmpakis and J. E. Millstone, *J. Am. Chem. Soc.*, 2015, **137**, 15852-15858.
62. Z. Farrell, S. Merz, J. Seager, C. Dunn, S. Egorov and D. L. Green, *Angew. Chem. Int. Ed.*, 2015, **54**, 6479-6482.
63. J. R. Reimers, M. J. Ford, A. Halder, J. Ulstrup and N. S. Hush, *Proc. Natl. Acad Sci. U. S. A.*, 2016, **113**, E1424-E1433.
64. Z. Farrell, C. Shelton, C. Dunn and D. Green, *Langmuir*, 2013, **29**, 9291-9300.
65. T. U. Dissanayake, M. Wang and T. J. Woehl, *Acs Appl. Mater. Interfaces*, 2021, **13**, 37553-37562.
66. J. Kang, Y.-X. Wang, F. Peng, N.-N. Zhang, Y. Xue, Y. Yang, E. Kumacheva and K. Liu, *Angew. Chem. Int. Ed.*, 2022, **61**, e202202405.
67. N. M. Schneider, M. M. Norton, B. J. Mendel, J. M. Grogan, F. M. Ross and H. H. Bau, *J. Phys. Chem. C*, 2014, **118**, 22373-22382.
68. J. H. Park, N. M. Schneider, J. M. Grogan, M. C. Reuter, H. H. Bau, S. Kodambaka and F. M. Ross, *Nano Lett.*, 2015, **15**, 5314-5320.
69. M. Wang, T. U. Dissanayake, C. Park, K. Gaskell and T. J. Woehl, *J. Am. Chem. Soc.*, 2019, **141**, 13516-13524.
70. J. Polte, *CrystEngComm*, 2015, **17**, 6809-6830.
71. Y. Yang, M. Romano, G. J. Feng, X. Z. Wang, T. Wu, S. Holdren and M. R. Zachariah, *Langmuir*, 2018, **34**, 585-594.
72. M. Zhou, H. L. Wang, M. Vara, Z. D. Hood, M. Luo, T. H. Yang, S. X. Bao, M. F. Chi, P. Xiao, Y. H. Zhang and Y. N. Xia, *J. Am. Chem. Soc.*, 2016, **138**, 12263-12270.
73. S. M. Ansar and C. L. Kitchens, *Acs Catal.*, 2016, **6**, 5553-5560.
74. R. D. Neal, R. A. Hughes, P. Sapkota, S. Ptasinska and S. Neretina, *Acs Catal.*, 2020, **10**, 10040-10050.
75. M. H. Luo, Y. C. Hong, W. F. Yao, C. P. Huang, Q. J. Xu and Q. Wu, *J. Mater. Chem. A*, 2015, **3**, 2770-2775.
76. Y. Zhong, L. Huang, J. Zhang, D. Xiang, P. Li, X. Yuan and M. Zhu, *Chem. Asian J.*, 2020, **15**, 1736-1742.
77. J. Priesner, T. Kraus and N. de Jonge, *Adv. Mater. Interfaces*, 2022, **9**, 2200699.
78. J. K. Pedersen, T. A. A. Batchelor, A. Bagger and J. Rossmeisl, *Acs Catal.*, 2020, **10**, 2169-2176.